

**Constraints on vector resonances from a strong Higgs sector**

A. E. Cárcamo Hernández,<sup>\*</sup> Bastián Díaz Sáez,<sup>†</sup> Claudio O. Dib,<sup>‡</sup> and Alfonso Zerwekh<sup>§</sup>  
*Department of Physics and Centro Científico-Tecnológico de Valparaíso Universidad Técnica Federico  
 Santa María, Valparaíso, Chile*

(Received 14 July 2017; published 26 December 2017)

We consider a scenario of a composite Higgs arising from a strong sector. We assume that the lowest lying composite states are the Higgs scalar doublet and a massive vector triplet, the dynamics below the compositeness scale of which are described in terms of an effective Lagrangian. Electroweak symmetry breaking takes place through a vacuum expectation value just as in the Standard Model, but with the vector resonances strongly coupled to the Higgs field. We determine the constraints on this scenario imposed by (i) the Higgs diphoton decay rate, (ii) the electroweak precision tests, and (iii) searches of heavy resonances at the LHC in the final states  $l^+l^-$  and  $l\nu_l$  ( $l = e, \mu$ ),  $\tau^+\tau^-$ ,  $jj$ ,  $t\bar{t}$ ,  $WZ$ ,  $WW$ ,  $WH$ , and  $ZH$ . We find that the heavy vector resonances should have masses in the range 2–3 TeV. In addition, the mixing of the heavy vectors with the Standard Model gauge bosons should be below  $\tan\vartheta \sim 0.3$ , which is consistent with the original assumption that the Higgs couples weakly to the Standard sector and strongly to the heavy vector resonances.

DOI: 10.1103/PhysRevD.96.115027

**I. INTRODUCTION**

The recent discovery of the Higgs boson at the LHC [1,2] provides the opportunity to directly explore the mechanism of electroweak symmetry breaking (EWSB). While this remarkable achievement implies severe constraints on many proposed extensions of the Standard Model (SM), an additional sector beyond our current knowledge is still needed in order to explain the dynamical origin of the electroweak scale and its stability [3]. A specific question in this context is whether this new sector is weakly or strongly interacting [4]. In the latter case, the Higgs boson is viewed as a composite state which must be accompanied by a plethora of new heavy composite particles [5–7]. In general, it is expected that the lightest states produced by the strong dynamics would correspond to spin-0 and spin-1 particles [5–8]. In these models, the lightness of the Higgs can be explained in two different ways. One way is to consider the Higgs boson as a pseudo-Goldstone boson that appears after the breakdown of a suitable global symmetry [6,7,9–26]. A second way is to consider the Higgs boson as the modulus of an effective  $SU(2)$  doublet, where its lightness is due to particularities of the dynamics of the underlying theory [16,27–58]. For instance, there are evidences that quasiconformal strong interacting theories such as walking technicolor may provide a light composite scalar [52–57]. It has also been shown that, in the effective low-energy theory, the composite scalar may develop a potential that reproduces the standard Higgs sector [27]. In this scheme, the electroweak symmetry breaking is

effectively described by a nonzero vacuum expectation value of the scalar arising from the potential, just as in the Standard Model. However, additional composite particles, like vector resonances, may also be expected to appear in the spectrum [59].

The main reason to consider strongly interacting mechanisms of EWSB as alternatives to the Standard Model mechanism based on a fundamental scalar is the so-called hierarchy problem that arises from the Higgs sector of the SM [5–7]. This problem is indicative that, in a natural scenario, new physics should appear at scales not much higher than the EWSB scale, say around a few TeV, in order to stabilize the Higgs mass at a value much lower than the Planck scale ( $\sim 10^{19}$  GeV). An underlying strongly interacting dynamics without fundamental scalars, which becomes nonperturbative somewhere above the electroweak scale, is a possible scenario that gives an answer to this problem.

While a composite Higgs boson is theoretically attractive because the underlying strong dynamics provides a comprehensive and natural explanation for the origin of the Fermi scale [5–7], the presence of additional composite states such as the vector triplets previously mentioned may, in principle, produce phenomenological problems. For instance, one could expect that, at one-loop level, they may produce sensible corrections to observables involving the Higgs boson. Consequently, an interesting quantity which can eventually reveal the influence of additional states is  $\Gamma(h \rightarrow \gamma\gamma)$ . In a previous work, this decay channel was studied in a simple model with vector resonances, and it was found it is in general agreement with current experimental measurements in the limit where the Higgs boson is weakly coupled to the new resonances [42]. However, if the Higgs boson arises from a strongly interacting sector together with other heavy resonances, one should expect a strong coupling among them.

<sup>\*</sup> antonio.carcamo@usm.cl

<sup>†</sup> bastian.diaz@alumnos.usm.cl

<sup>‡</sup> claudio.dib@usm.cl

<sup>§</sup> alfonso.zerwekh@usm.cl

In this work, we want to investigate whether this strong coupling hypothesis is still compatible with the currently known phenomenology and, in general, whether composite models are viable alternatives to electroweak symmetry breaking, given the current experimental success of the Standard Model [3]. To be concrete, we describe the new sector by means of an effective model with minimal particle content, without referring to the details of the underlying strong dynamics. We use an effective chiral Lagrangian to describe the theory below the cutoff scale of the underlying strong interaction, assumed to be  $\Lambda = 4\pi v \sim 3$  TeV. This low-energy effective theory must contain the Standard Model spectrum and the extra composite scalar and vector multiplets.

The content of this paper goes as follows. In Sec. II, we introduce our effective Lagrangian that describes the spectrum of the theory. Section III deals with the constraints arising from the Higgs diphoton decay rate. The constraints on the model parameter space arising from the oblique  $T$  and  $S$  parameters are discussed in Sec. IV. In Sec. V, we describe the different production and decay channels of the heavy vector resonances. In Sec. VI, we present the constraints of our model arising from LHC searches of heavy vector resonances. Finally, in Sec. VII, we state our conclusions.

## II. LAGRANGIAN FOR A HIGGS DOUBLET AND HEAVY VECTOR TRIPLET

We want to formulate the scenario of EWSB triggered by a strongly coupled sector without referring to specific details of the underlying theory. This underlying theory, as it becomes strong at low energies, should generate the Higgs scalar multiplet as a composite field below a scale  $\Lambda \sim 4\pi v$ , where  $v$  will be the analog of the pion decay constant in QCD. We will assume that, in addition to the composite scalar multiplet, there will remain a vector composite multiplet below the scale  $\Lambda$ . One should then expect that these composite fields would exhibit a remnant strong coupling among themselves, which is the main hypothesis we want to test.

We will assume the vector composites to form a triplet under  $SU(2)_L$ , while the scalars will form a Higgs doublet just as in the SM. To this end, we construct the effective theory based on a hidden local  $SU(2)$  symmetry so that our gauge group appears as  $SU(2)_1 \times SU(2)_2 \times U(1)_Y$ . To give large masses to the vectors, the  $SU(2)_1 \times SU(2)_2$  part will be broken down to the diagonal subgroup, i.e., the standard  $SU(2)_L$ . The would-be Goldstone bosons of this breaking will be incorporated as a nonlinear sigma model field  $\Sigma$ . In turn, the gauge symmetry of the Standard Model will be broken, as usual, when the electrically neutral component of the scalar doublet  $\Phi$  acquires a vacuum expectation value.

We denote the gauge fields of  $SU(2)_1$ ,  $SU(2)_2$ , and  $U(1)_Y$  as  $A_\mu^{(1)}$ ,  $A_\mu^{(2)}$ , and  $B_\mu$ , respectively. After the breaking

TABLE I. Field charge assignments under the full gauge group  $SU(2)_1 \times SU(2)_2 \times U(1)_Y$ . The  $i$  index runs from 1 to 3.

Fields	$SU(2)_1$	$SU(2)_2$	$U(1)_Y$
$\Sigma$	<b>2</b>	$\bar{\mathbf{2}}$	0
$\Phi$	1	<b>2</b>	1/2
$Q_L^i$	<b>2</b>	1	1/6
$U_R^i$	1	1	2/3
$D_R^i$	1	1	-1/3
$L_L^i$	<b>2</b>	1	-1/2
$e_R^i$	1	1	-1
$N_R^i$	1	1	0

of  $SU(2)_1 \times SU(2)_2 \rightarrow SU(2)_L$ , one combination of the vector fields  $A_\mu^{(1)}$  and  $A_\mu^{(2)}$  will become the heavy vectors, and the other combination will remain as the  $SU(2)_L$  gauge fields. In our notation, the heavy vectors will be mainly  $A_\mu^{(2)}$  with a small admixture of  $A_\mu^{(1)}$ . The scalar doublet  $\Phi$ , i.e., the Higgs field for the SM, on the other hand, should be completely localized at the  $SU(2)_2$  site, in order to reflect a stronger coupling to the heavy vectors. As such,  $\Sigma$  is a doublet under both  $SU(2)_1$  and  $SU(2)_2$ , while  $\Phi$  and  $\psi_{iL}$  are doublets only under  $SU(2)_2$  and  $SU(2)_1$ , respectively (see Table I). The effective Lagrangian is expressed as

$$\begin{aligned}
\mathcal{L} = & -\frac{1}{2} \langle F_{\mu\nu}^{(1)} F^{(1)\mu\nu} \rangle - \frac{1}{2} \langle F_{\mu\nu}^{(2)} F^{(2)\mu\nu} \rangle - \frac{1}{2} \langle B_{\mu\nu} B^{\mu\nu} \rangle \\
& + \frac{f_\Sigma^2}{2} \langle (D_\mu \Sigma)^\dagger D^\mu \Sigma \rangle + (D_\mu \Phi)^\dagger D^\mu \Phi - \mu^2 \Phi^\dagger \Phi \\
& + \frac{\lambda}{4} (\Phi^\dagger \Phi)^2 + \frac{\beta}{2} (\Phi^\dagger \Phi) \langle (D_\mu \Sigma)^\dagger D^\mu \Sigma \rangle + i\bar{\psi}_{iL} \gamma^\mu D_\mu \psi_{iL} \\
& + i\bar{\psi}_{iR} \gamma^\mu D_\mu \psi_{iR} + y_{ij} \bar{\psi}_{iL} \Sigma \Phi \psi_{iR} + \tilde{y}_{ij} \bar{\psi}_{iL} \Sigma \Phi^c \psi_{iR} \\
& + \text{H.c.}
\end{aligned} \tag{1}$$

Here  $F^{(1)\mu\nu}$ ,  $F^{(2)\mu\nu}$ , and  $B^{\mu\nu}$  are the gauge field tensors; the brackets  $\langle \rangle$  denote the trace in the corresponding group indices;  $f_\Sigma$  is the analog of a decay constant for the extra would-be Goldstones expressed nonlinearly in the field  $\Sigma$  (these are absorbed as the longitudinal components of the heavy vector composites);  $\lambda$  and  $\mu$  are the SM parameters of the Higgs potential; and  $\beta$  is the coefficient of a mixing term allowed by the symmetry. The value of  $\beta$  is not easy to isolate from other parameters in observable quantities, so we scan values of  $\beta$  of order unity, in the range  $-4$  to  $+4$ . Finally, the covariant derivatives are

$$\begin{aligned}
D_\mu \Sigma &= \partial_\mu \Sigma - ig_1 A_\mu^{(1)} \Sigma + ig_2 \Sigma A_\mu^{(2)}, \\
D_\mu \Phi &= \partial_\mu \Phi - ig_2 A_\mu^{(2)} \Phi - i\frac{g'}{2} B_\mu \Phi, \\
D_\mu \psi_{iL} &= \partial_\mu \psi_{iL} - ig_1 A_\mu^{(1)} \psi_{iL} - ig' Y_{f_{iL}} B_\mu \psi_{iL}, \\
D_\mu \psi_{iR} &= \partial_\mu \psi_{iR} - ig' Y_{f_{iR}} B_\mu \psi_{iR},
\end{aligned} \tag{2}$$

where  $A_\mu^{(n)} = \frac{1}{2}\tau^a A_\mu^{(n)a}$  ( $n = 1, 2$ ) are the Hermitian gauge field matrices corresponding to the  $SU(2)_n$  gauge fields  $A_\mu^{(n)}$ ,  $n = 1, 2$ , respectively.

Notice that  $\Phi$  is coupled to  $A_\mu^{(2)}$  but not to  $A_\mu^{(1)}$ , and so it is more strongly coupled to the heavy vectors than to the SM gauge fields. In addition, left-handed SM fermionic fields will couple mainly to SM gauge fields, which are primarily contained in  $SU(2)_1$ . The scalar doublet will correspond to the SM Higgs field, which can be expressed as usual by

$$\Phi = \begin{pmatrix} G^+ \\ \frac{1}{\sqrt{2}}(v + h + iG^0) \end{pmatrix}, \quad (3)$$

where the field  $h$  is the Higgs boson, while  $G^\pm$  and  $G^0$  are the would-be Goldstones that will be absorbed after EWSB. The spontaneous breaking of the extra gauge symmetry can be formulated by taking  $\Sigma = 1$  (in the unitary gauge). The Lagrangian then takes the form

$$\begin{aligned} \mathcal{L} = & \mathcal{L}_{\text{gauge}} + \frac{f_\Sigma^2 g^2}{4\sin^2 2\vartheta} V_\mu^{(2)} V^{(2)\mu} + (D_\mu \Phi)^\dagger D^\mu \Phi - \mu^2 \Phi^\dagger \Phi \\ & + \frac{\lambda}{4} (\Phi^\dagger \Phi)^2 + \frac{\beta g^2}{\sin^2 2\vartheta} (\Phi^\dagger \Phi) V_\mu^{(2)} V^{(2)\mu} + i\bar{\psi}_{iL} \gamma^\mu D_\mu \psi_{iL} \\ & + i\bar{\psi}_{iR} \gamma^\mu D_\mu \psi_{iR} + y_{ij} \bar{\psi}_{iL} \Phi \psi_{jR} + \tilde{y}_{ij} \bar{\psi}_{iL} \Phi^c \psi_{jR} + \text{H.c.}, \end{aligned} \quad (4)$$

where the covariant derivative is now rewritten as

$$D_\mu \Phi = \partial_\mu \Phi - ig \frac{\tau^a}{2} V_{\mu,a}^{(1)} \Phi - i\tilde{g} \frac{\tau^a}{2} V_{\mu,a}^{(2)} \Phi - i \frac{g'}{2} B_\mu \Phi, \quad (5)$$

with the vector fields given by

$$\begin{aligned} V_\mu^{(1)} &= \cos \vartheta A_\mu^{(1)} + \sin \vartheta A_\mu^{(2)}, \\ V_\mu^{(2)} &= -\sin \vartheta A_\mu^{(1)} + \cos \vartheta A_\mu^{(2)}, \quad \tan \vartheta = \frac{g_1}{g_2} \end{aligned} \quad (6)$$

and the couplings

$$g = \frac{g_1 g_2}{\sqrt{g_1^2 + g_2^2}}, \quad \tilde{g} = \frac{g_2^2}{\sqrt{g_1^2 + g_2^2}}. \quad (7)$$

At this stage, the fields  $V_\mu^{(1)}$  remain massless, but  $V_\mu^{(2)}$  acquire mass proportional to  $f_\Sigma$ , as shown in Eq. (4). When the Higgs boson acquires a vacuum expectation value  $\langle \Phi \rangle = \frac{1}{\sqrt{2}}(0, v)^T$ , from Eq. (4), it follows that the squared mass matrices for the neutral and charged gauge bosons are given by

$$\begin{aligned} M_N^2 &= \frac{v^2}{4} \begin{pmatrix} g^2 & -gg' & g\tilde{g} \\ -gg' & g^2 & -g'\tilde{g} \\ g\tilde{g} & -g'\tilde{g} & \tilde{g}^2 k^2 \end{pmatrix}, \quad M_C^2 = \frac{v^2}{4} \begin{pmatrix} g^2 & g\tilde{g} \\ g\tilde{g} & k^2 \tilde{g}^2 \end{pmatrix}, \\ & \text{with } k^2 = 1 + \frac{2f_\Sigma^2 + \beta v^2}{v^2 \cos^4 \vartheta}. \end{aligned} \quad (8)$$

The masses of the gauge bosons are given by diagonalization of these mass matrices,

$$\begin{aligned} M_A &= 0, \\ M_Z &= \frac{v}{2\sqrt{2}} \sqrt{g^2 + g^2 + \tilde{g}^2 k^2 - \sqrt{\tilde{g}^4 k^4 + (g^2 + g^2)[g^2 + g^2 + 2(2 - k^2)\tilde{g}^2]}}, \\ M_{\rho^0} &= \frac{v}{2\sqrt{2}} \sqrt{g^2 + g^2 + \tilde{g}^2 k^2 + \sqrt{\tilde{g}^4 k^4 + (g^2 + g^2)[g^2 + g^2 + 2(2 - k^2)\tilde{g}^2]}}, \\ M_{W^\pm} &= \frac{v}{2\sqrt{2}} \sqrt{k^2 \tilde{g}^2 + g^2 - \sqrt{(g^2 - k^2 \tilde{g}^2)^2 + 4g^2 \tilde{g}^2}}, \\ M_{\rho^\pm} &= \frac{v}{2\sqrt{2}} \sqrt{k^2 \tilde{g}^2 + g^2 + \sqrt{(g^2 - k^2 \tilde{g}^2)^2 + 4g^2 \tilde{g}^2}}, \end{aligned} \quad (9)$$

and the physical neutral and charged gauge bosons are given by

$$\begin{pmatrix} A_\mu \\ Z_\mu \\ \rho_\mu^0 \end{pmatrix} = \begin{pmatrix} \cos \theta_W & \sin \theta_W & 0 \\ -\cos \gamma \sin \theta_W & \cos \gamma \cos \theta_W & -\sin \gamma \\ -\sin \gamma \sin \theta_W & \cos \theta_W \sin \gamma & \cos \gamma \end{pmatrix} \begin{pmatrix} B_\mu^0 \\ V_{\mu,3}^{(1)} \\ V_{\mu,3}^{(2)} \end{pmatrix}, \quad \begin{pmatrix} W_\mu^\pm \\ \rho_\mu^\pm \end{pmatrix} = \begin{pmatrix} \cos \kappa & -\sin \kappa \\ \sin \kappa & \cos \kappa \end{pmatrix} \begin{pmatrix} V_\mu^{(1)\pm} \\ V_\mu^{(2)\pm} \end{pmatrix}, \quad (10)$$

where, besides the standard  $\theta_W$ , the additional mixing angles  $\kappa$  and  $\gamma$  are

$$\begin{aligned}\tan 2\kappa &= \frac{\sqrt{(4M_{\rho^\pm}^2 - g^2 v^2)(g^2 v^2 - 4M_W^2)}}{2(M_{\rho^\pm}^2 + M_W^2) - g^2 v^2}, \\ \tan 2\gamma &= \frac{2\tilde{g}\sqrt{g^2 + g'^2}}{\tilde{g}^2 k^2 - g^2 - g'^2}.\end{aligned}\quad (11)$$

At this stage, the electroweak symmetry is finally broken, and the only remaining massless vector boson is the photon field  $A_\mu$ .

### III. CONSTRAINTS FROM HIGGS DECAY INTO TWO PHOTONS

In the Standard Model, the  $h \rightarrow \gamma\gamma$  decay is dominated by  $W$  loop diagrams which can interfere destructively with the subdominant top quark loop. In our strongly coupled model, the  $h \rightarrow \gamma\gamma$  decay receives additional contributions from loops with charged  $\rho_\mu^\pm$ , as shown in Fig. 1. The explicit form for the  $h \rightarrow \gamma\gamma$  decay rate is

$$\begin{aligned}\Gamma(h \rightarrow \gamma\gamma) &= \frac{\alpha_{em}^2 m_h^3}{256\pi^3 v^2} \left| \sum_f N_c Q_f^2 F_{1/2}(x_f) \right. \\ &\quad \left. + a_{hWW} F_1(x_W) + a_{h\rho^+\rho^-} F_1(x_\rho) \right|^2,\end{aligned}\quad (12)$$

where

$$a_{hW^+W^-} = \frac{vg^2}{2} \left\{ (\cos\kappa - \cot\vartheta \sin\kappa)^2 + \frac{\beta \sin^2\kappa}{\sin^2\vartheta \cos^2\vartheta} \right\} \frac{v}{2M_W^2},\quad (13)$$

$$a_{h\rho^+\rho^-} = \frac{vg^2}{2} \left\{ (\sin\kappa + \cot\vartheta \cos\kappa)^2 + \frac{\beta \cos^2\kappa}{\sin^2\vartheta \cos^2\vartheta} \right\} \frac{v}{2M_{\rho^\pm}^2}.\quad (14)$$

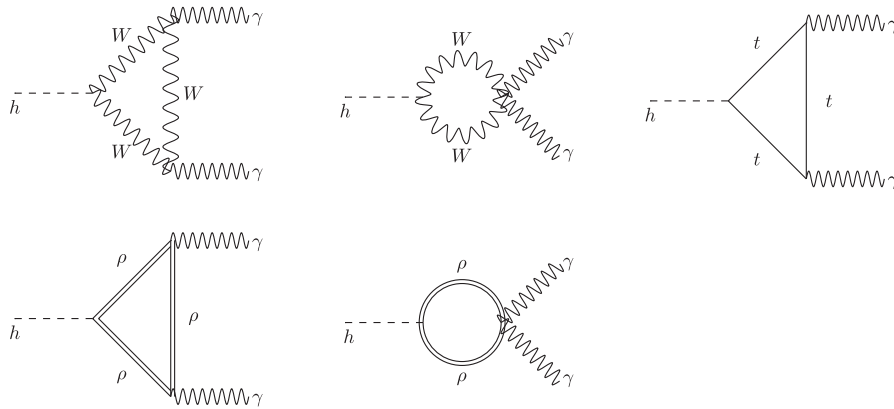


FIG. 1. One-loop Feynman diagrams in the unitary gauge contributing to the  $h \rightarrow \gamma\gamma$  decay.

Here,  $x_f = m_h^2/4m_f^2$ ,  $x_W = m_h^2/4M_W^2$  and  $x_\rho = m_h^2/4M_\rho^2$ ;  $\alpha_{em}$  is the fine structure constant;  $N_C$  is the color factor ( $N_C = 1$  for leptons and  $N_C = 3$  for quarks); and  $Q_f$  is the electric charge of the fermion in the loop. From the fermion loop contributions, we will keep only the dominant term, which is the one involving the top quark.

The dimensionless loop factors  $F_{1/2}(x)$  and  $F_1(x)$  (for particles of spin 1/2 and 1 in the loop, respectively) are [60–67]

$$F_{1/2}(x) = 2[x + (x-1)f(x)]x^{-2},\quad (15)$$

$$F_1(x) = -[2x^2 + 3x + 3(2x-1)f(x)]x^{-2},\quad (16)$$

with

$$f(x) = \begin{cases} \arcsin^2 \sqrt{x}, & \text{for } x \leq 1 \\ -\frac{1}{4} \left[ \ln \left( \frac{1+\sqrt{1-x^{-1}}}{1-\sqrt{1-x^{-1}}} \right) - i\pi \right]^2, & \text{for } x > 1. \end{cases}\quad (17)$$

In what follows, we want to determine the range of values for the mass  $M_\rho$  of the heavy vector resonances and the mixing angle  $\vartheta$ , consistent with the Higgs diphoton signal strength measured by the ATLAS and CMS collaborations at the LHC. To this end, we introduce the ratio  $R_{\gamma\gamma}$ , which corresponds to the Higgs diphoton signal strength that normalizes the  $\gamma\gamma$  signal predicted by our model relative to that of the SM:

$$R_{\gamma\gamma} = \frac{\sigma(pp \rightarrow h)\Gamma(h \rightarrow \gamma\gamma)}{\sigma(pp \rightarrow h)_{\text{SM}}\Gamma(h \rightarrow \gamma\gamma)_{\text{SM}}} \simeq \frac{\Gamma(h \rightarrow \gamma\gamma)}{\Gamma(h \rightarrow \gamma\gamma)_{\text{SM}}}.$$

This normalization for  $h \rightarrow \gamma\gamma$  was also done in Refs. [67–69]. Here, we have used the fact that in our model single Higgs production is also dominated by gluon fusion as in the Standard Model.

Figure 2 shows the sensitivity of the ratio  $R_{\gamma\gamma}$  under variations of  $M_\rho$  for several values of  $\tan\vartheta$ . The curves

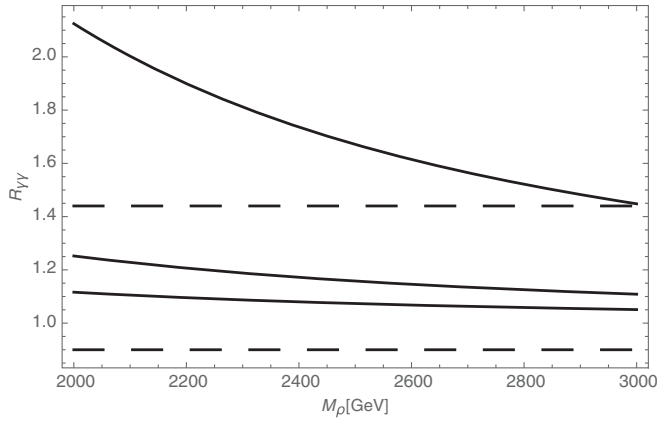


FIG. 2. The ratio  $R_{\gamma\gamma}$  as a function of  $M_\rho$  for several values of  $\tan\vartheta$ . The solid curves from top to bottom correspond to  $\tan\vartheta = 0.1, 0.2,$  and  $0.3$ . The horizontal dashed lines are the minimum and maximum values of the ratio  $R_{\gamma\gamma}$  inside the  $1\sigma$  experimentally allowed range by CMS and ATLAS, namely,  $1.14^{+0.26}_{-0.23}$  and  $1.17 \pm 0.27$ , respectively [70,71].

from top to bottom correspond to  $\tan\vartheta = 0.1, 0.2, 0.3$ . The ratio  $R_{\gamma\gamma}$  decreases slowly when the heavy vector masses are increased.

As shown, our model successfully accommodates the current Higgs diphoton decay rate constraints.

A more exhaustive study of the allowed values of  $\vartheta$  for different  $M_\rho$  and several values of  $\beta$  is shown in Fig. 3. The observed Higgs diphoton decay rate at the LHC excludes the region below the respective curve in the figure, corresponding to too-small values of  $\vartheta$ ; for such small  $\vartheta$  values, the Higgs boson would couple too strongly to the heavy vector resonances, increasing the Higgs diphoton decay rate beyond the observed values. In addition, the heavy vector contribution to the Higgs diphoton decay rate scales as  $1/M_\rho^2$  due to the heavy vector propagator, and consequently, as Fig. 3 shows, the tightest lower bounds for  $\tan\vartheta$  are obtained at lower  $M_\rho$  values. It is worth

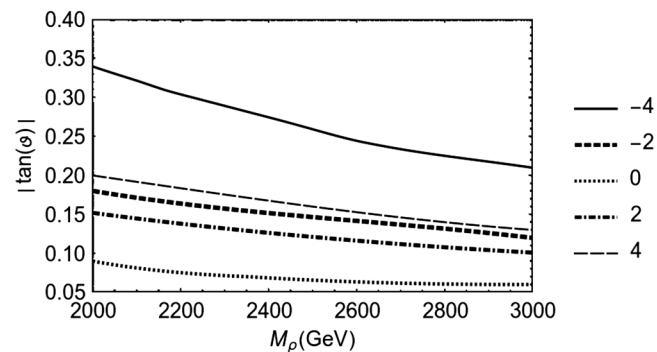


FIG. 3. Lower bound on  $\tan\vartheta$  vs  $M_\rho$ , for different values of the Lagrangian parameter  $\beta$ , cf. Eq. (1), according to the constraint imposed by the Higgs diphoton decay rate  $h \rightarrow \gamma\gamma$  at the LHC. For each value of  $\beta$ , the region below the respective curves is excluded.

mentioning that for larger positive  $\beta$  the coupling of the Higgs boson to the heavy vector resonances increases, potentially going over the LHC upper bound, thus requiring larger  $\tan\vartheta$ . On the other hand, for more and more negative  $\beta$ , the coupling of the Higgs to vector resonances decreases, potentially going below the LHC lower bound, thus requiring again larger values of  $\tan\vartheta$ . Indeed, as Fig. 3 shows, the lowest bounds on  $\tan\vartheta$  are reached for  $\beta = 0$ .

#### IV. CONSTRAINTS FROM THE $T$ AND $S$ PARAMETERS

The inclusion of the extra composite particles also modifies the oblique corrections of the SM, the values of which have been extracted from high-precision experiments. Consequently, the validity of our model depends on the condition that the extra particles do not contradict those experimental results. These oblique corrections are parametrized in terms of the two well-known quantities  $T$  and  $S$ . The  $T$  parameter is defined as [72–74]

$$T = \frac{\Pi_{33}(0) - \Pi_{11}(0)}{M_W^2 \alpha_{em}(m_Z)}, \quad (18)$$

where  $\Pi_{33}(0)$  and  $\Pi_{11}(0)$  are the vacuum polarization amplitudes at  $q^2 = 0$  for the propagators of the gauge bosons  $A_{\mu,3}^{(1)}$  and  $A_{\mu,1}^{(1)}$ , respectively, which are those that couple to the external fermions in the process  $e^+e^- \rightarrow f\bar{f}$  [74].

In turn, the  $S$  parameter is defined as [72–74]

$$S = \frac{4\sin^2\theta_W}{\alpha_{em}(m_Z)} \frac{g}{g'} \frac{d}{dq^2} \Pi_{30}(q^2) \Big|_{q^2=0}, \quad (19)$$

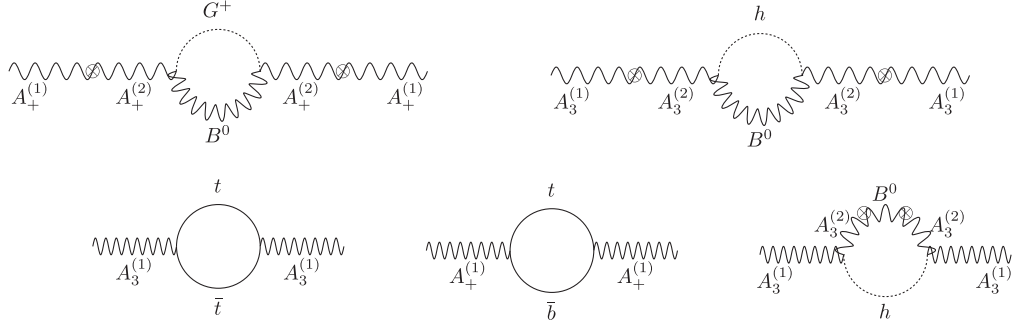
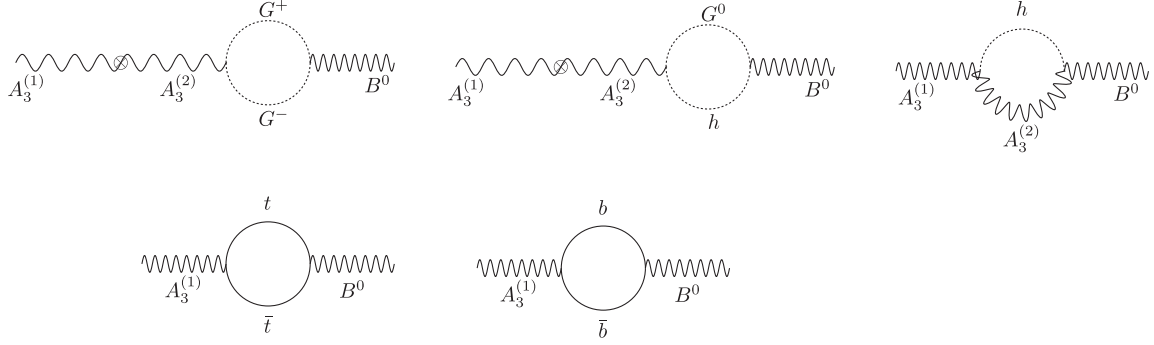
where  $\Pi_{30}(q^2)$  is the vacuum polarization for the propagator mixing of  $A_{\mu,3}^{(1)}$  and  $B_\mu$ . The most important Feynman diagrams contributing to the  $T$  and  $S$  parameters are shown in Figs. 4 and 5. We computed these oblique  $T$  and  $S$  parameters in the Landau gauge for the SM gauge bosons and would-be-Goldstone bosons, in which the global  $SU(2)_L \times U(1)_Y$  symmetry is preserved. We can separate the contributions to  $T$  and  $S$  from the SM and extra physics as  $T = T_{\text{SM}} + \Delta T$  and  $S = S_{\text{SM}} + \Delta S$ , where

$$T_{\text{SM}} = -\frac{3}{16\pi\cos^2\theta_W} \ln\left(\frac{m_h^2}{m_W^2}\right) + \frac{3m_t^2}{32\pi^2\alpha_{em}(m_Z)v^2},$$

$$S_{\text{SM}} = \frac{1}{12\pi} \ln\left(\frac{m_h^2}{m_W^2}\right) + \frac{1}{2\pi} \left[ 3 - \frac{1}{3} \ln\left(\frac{m_t^2}{m_b^2}\right) \right], \quad (20)$$

while  $\Delta T$  and  $\Delta S$  contain all the contributions involving the extra particles.

The tree and dominant one-loop contributions to  $\Delta T$  and  $\Delta S$  in our model are


 FIG. 4. One-loop Feynman diagrams contributing to the  $T$  parameter. The fields are those in Eqs. (2) and (3).

 FIG. 5. One-loop Feynman diagrams contributing to the  $S$  parameter. The fields are those in Eqs. (2) and (3).

$$\Delta T = \frac{v^8 \tan^2 \vartheta \tan^2 \theta_W}{256 \alpha_{em} (m_Z) M_W^4 M_\rho^4} + \tan^2 \vartheta T_{SM} - \frac{3\beta^2 M_W^4}{16\pi \cos^2 \vartheta \sin^4 \vartheta \cos^2 \theta_W} F(M_W \tan \theta_W, m_h, M_{A^{(2)}}), \quad (21)$$

$$\Delta S = \frac{v^4 \tan^2 \vartheta \sin^2 \theta_W}{4\alpha_{em} (m_Z) \cos^3 \vartheta M_W^2 M_\rho^2} + \frac{1 - \cos \vartheta}{\cos \vartheta} S_{SM} + \frac{2\beta M_W^2}{\pi \sin^2 \vartheta \cos \vartheta} \left[ G_1(M_{A^{(2)}}, m_h) - \frac{1}{4M_{A^{(2)}}^2} G_2(M_{A^{(2)}}, m_h) \right], \quad (22)$$

where

$$F(m_1, m_2, m_3) = \frac{m_1^2}{(m_1^2 - m_2^2)(m_1^2 - m_3^2)} \ln \left( \frac{1 + \Lambda^2/m_1^2}{1 + \Lambda^2/m_3^2} \right) + \frac{m_2^2}{(m_2^2 - m_1^2)(m_2^2 - m_3^2)} \ln \left( \frac{1 + \Lambda^2/m_2^2}{1 + \Lambda^2/m_3^2} \right) + \frac{m_3^2}{(m_3^2 - m_1^2)(m_3^2 - m_2^2)} \left[ \frac{1}{\Lambda^2 + m_3^2} - \frac{1}{m_3^2} \right], \quad (23)$$

$$G_1(m_1, m_2) = \int_0^1 dx x(1-x) \left[ \frac{\frac{1}{2}[-(m_1^2 - m_2^2)x + m_1^2] + \Lambda^2}{([\Lambda^2 - (m_1^2 - m_2^2)x + m_1^2] + \Lambda^2)^2} - \frac{1}{2[-(m_1^2 - m_2^2)x + m_1^2]} \right], \quad (24)$$

$$G_2(m_1, m_2) = \int_0^1 dx x(1-x) \left[ \ln \left( \frac{\Lambda^2 + [-(m_1^2 - m_2^2)x + m_1^2]}{[-(m_1^2 - m_2^2)x + m_1^2]} \right) - \frac{3}{2} \right] + \int_0^1 dx x(1-x) \frac{4[-(m_1^2 - m_2^2)x + m_1^2] \Lambda^2 + 3[-(m_1^2 - m_2^2)x + m_1^2]^2}{2\{\Lambda^2 + [-(m_1^2 - m_2^2)x + m_1^2]\}^2}, \quad (25)$$

$$M_{A^{(2)}} = \frac{g_2}{\sqrt{2}} \sqrt{f_\Sigma^2 + \frac{\beta+1}{2} v^2} \simeq \frac{4\cos^2 \vartheta}{\sin \vartheta} \left( \frac{M_W}{v} \right)^2 M_\rho. \quad (26)$$

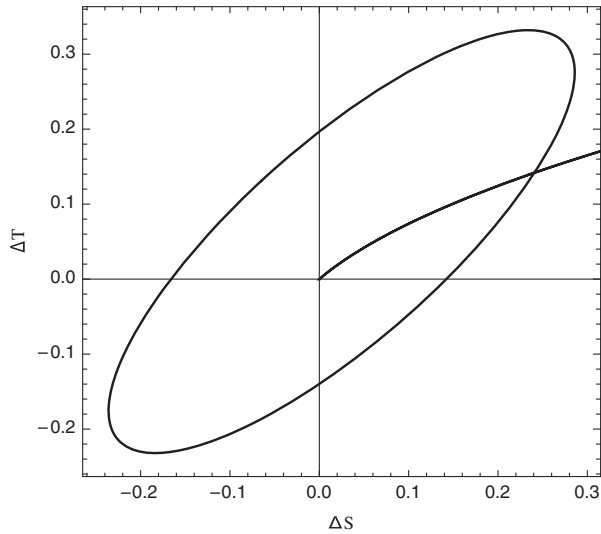


FIG. 6. The  $\Delta S$ - $\Delta T$  plane in our model. The ellipses denote the experimentally allowed region at 95% C.L. taken from Ref. [75]. The origin  $\Delta S = \Delta T = 0$  corresponds to the Standard Model value, with  $m_h = 126$  GeV and  $m_t = 176$  GeV. The line coming from the origin shows the values of  $\Delta S$  and  $\Delta T$  in the model, as  $\tan \theta$  varies over the range  $0 \leq \tan \theta \leq 0.6$  and the heavy vector mass is kept fixed at 2 TeV. The line coming from the origin intersects the ellipse at  $\tan \theta \sim 0.5$ , thus the upper bound of  $\tan \theta$ .

We computed the tree-level contribution to the  $T$  parameter from the relation  $\alpha_{em}(m_Z)T_{tree} = \frac{M_W^2}{M_Z^2 \cos^2 \theta_W} - 1$ , where Eq. (9) was used.

As a result, the experimental constraints on the  $T$  and  $S$  parameters [75] impose an upper bound on our mixing parameter  $\tan \theta \lesssim 0.5$ , for heavy vector masses from 2 up to 3 TeV (see Fig. 6).

The lack of  $M_\rho$  dependence of the upper bound  $\tan \theta \lesssim 0.5$  arising from the oblique parameters  $T$  and  $S$  can be explained as follows. The tree-level contributions to  $T$  and  $S$  from the vector resonances go as  $v^4/M_\rho^4$  and  $v^2/M_\rho^2$ , respectively, which are small for the vector masses  $M_\rho$  we are considering, namely, larger than about 2 TeV. The one-loop contributions of the heavy vectors to  $T$  are thus dominant, and these are described by the loop functions  $F(M_W \tan \theta_W, m_h, M_{A^{(2)}})$ ,  $G_1(M_{A^{(2)}}, m_h)$ , and  $G_2(M_{A^{(2)}}, m_h)$ , which have low sensitivity for cases in which  $M_\rho$  are much larger than the Higgs boson mass, as is the case here. In what regards the  $S$  parameter, the tree-level contribution to this parameter becomes dominant with respect to its one loop-level contribution. However, due to the fact that we are considering heavy vector masses larger than about 2 TeV, our model pass the electroweak precision constraints provided that  $\tan \theta \lesssim 0.5$

Consequently, here,  $T$  and  $S$  have a very weak dependence on  $M_\rho$ .

We have also verified numerically that the upper bound  $\tan \theta \lesssim 0.5$ , arising from  $T$  and  $S$ , does not change when  $\beta$  is varied over the range  $-4 \leq \beta \leq 4$ . This is indeed the case

because the one loop-level contributions are small for heavy vector masses larger than about 2 TeV.

Finally, it is worth mentioning that the obtained values for  $T$  and  $S$  in our model coincide with the predictions of the SM for a vanishing  $\tan \theta$  because, in the limit  $\tan \theta \rightarrow 0$ ,  $M_{A^{(2)}}$  become extremely large [see Eq. (26)], and thus the heavy vectors are decoupled from the theory.

## V. PRODUCTION AND DECAYS OF THE HEAVY VECTORS

The current important period of LHC exploration of the Higgs properties and discovery of heavier particles may provide crucial steps to unravel the electroweak symmetry breaking mechanism. Consequently, we complement our work by studying the production and decay channels of the heavy vector resonances which are relevant for the LHC.

At a hadron collider like the LHC, the most important production channel for the heavy vector resonance is quark-antiquark annihilation. In our construction, the coupling of heavy vectors to quarks goes through a term which has its origin in the mixing between the gauge fields  $A_\mu^{(1)}$  and  $A_\mu^{(2)}$ . Consequently, the  $\rho$  production amplitude is proportional to  $\tan \theta$ , which acts as a suppression factor. The influence of  $\tan \theta$  can be seen in Fig. 7, in which we show the  $\rho$  production cross section, computed with CALCHEP [76], for different values of  $M_\rho$  and  $\tan \theta$ .

Additionally, we compute the two-body decay rates of the heavy vectors. These rates, up to corrections of order  $m_h^2/M_\rho^2$  and  $M_W^2/M_\rho^2$ , are

$$\begin{aligned} \Gamma(\rho^0 \rightarrow q\bar{q}) &\simeq \frac{3g^2 \tan^2 \theta}{96\pi} M_\rho, \\ \Gamma(\rho^+ \rightarrow u_i \bar{d}_j) &= \Gamma(\rho^- \rightarrow \bar{u}_i d_j) \simeq \frac{3g^2 \tan^2 \theta}{96\pi} |V_{ij}|^2 M_\rho, \\ \Gamma(\rho^\pm \rightarrow W^\pm h) &= \Gamma(\rho^0 \rightarrow Zh) \simeq \frac{g^2 \cot^2 \theta}{96\pi} M_\rho, \\ \Gamma(\rho^0 \rightarrow W^+ W^-) &= \Gamma(\rho^\pm \rightarrow W^\pm Z) \simeq \frac{g^2 \cot^2 \theta}{96\pi} M_\rho. \end{aligned} \quad (27)$$

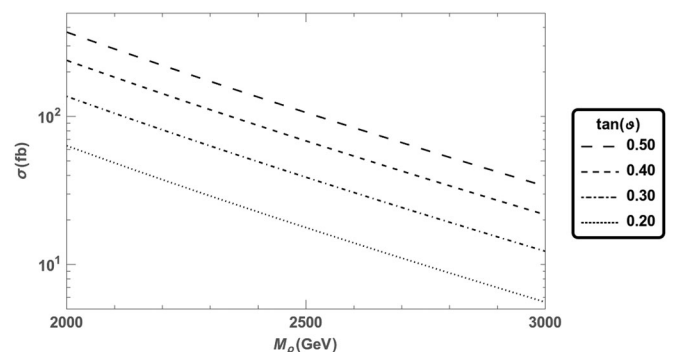


FIG. 7. Heavy vector production cross section  $\sigma(pp \rightarrow \rho)$  vs  $M_\rho$ , for  $\tan \theta = 0.2, 0.3, 0.4$  and  $0.5$ .

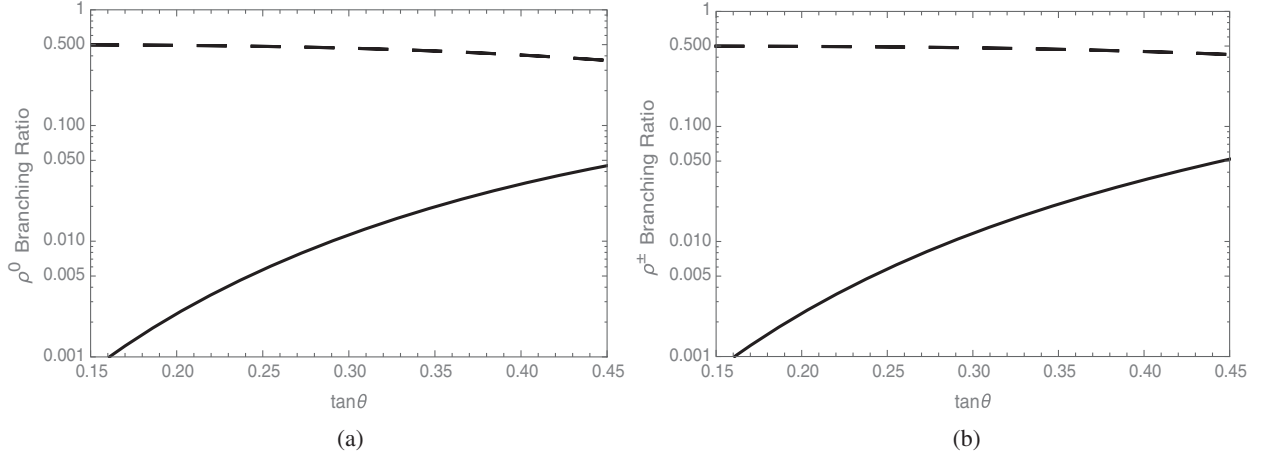


FIG. 8. Branching ratios of neutral and charged heavy vector decays vs  $\tan \vartheta$ : (a) neutral vector decays:  $\text{Br}(\rho^0 \rightarrow q\bar{q})$ ,  $q = u, d, s, \dots$  (solid) and  $\text{Br}(\rho^0 \rightarrow W^+W^-) = \text{Br}(\rho^0 \rightarrow Zh)$  (dashed); (b) charged vector decays:  $\text{Br}(\rho^+ \rightarrow u\bar{d}) = \text{Br}(\rho^- \rightarrow d\bar{u})$  (solid) and  $\text{Br}(\rho^\pm \rightarrow W^\pm Z) = \text{Br}(\rho^\pm \rightarrow W^\pm h)$  (dashed).

Figure 8 displays the branching ratios of the neutral (a) and charged (b) heavy vectors to a quark-antiquark pair and to a SM-like Higgs in association with a SM gauge boson, as a function of  $\tan \vartheta$ . This angle controls the strength of the coupling of the heavy vector resonances with fermions. Clearly the largest decay rates of the heavy vectors are into a pair of SM gauge bosons as well as into a SM-like Higgs and SM gauge boson, for all values of  $\tan \vartheta$ . The decays into quark-antiquark pairs are much smaller in the relevant region of parameter space. This is a direct consequence of the gauge structure of the model and the representations of the fermions and the Higgs doublet under the full gauge symmetry group.

## VI. BOUNDS FROM LHC SEARCHES

The ATLAS and CMS collaborations have performed several searches for heavy resonances decaying into

different final states [77–81]. These searches are based on upper limits in the resonant cross section for different heavy vector particles. We use those limits to set restrictions on the model parameter space, thus complementing the diphoton and the electroweak precision test constraints described above. As stated at the end of Secs. III and IV, the allowed mixing parameter  $\tan \vartheta$  is restricted to the range  $0.15 \lesssim \tan \vartheta \lesssim 0.5$ . In what follows, we will use as benchmark points the values  $\tan \vartheta = 0.15, 0.20, 0.30$ , and  $0.50$ .

We now focus on the LHC upper limits to constrain the model parameter space using the final states  $l^+l^-$ ,  $l\nu_l$  ( $l = e, \mu$ ),  $\tau^+\tau^-$ ,  $jj$ ,  $t\bar{t}$ ,  $WZ$ ,  $WW$ ,  $WH$ , and  $ZH$ , assumed to be produced through a resonant  $\rho^0$  or  $\rho^\pm$  decay. For example, the observation of the combined dilepton modes  $e^+e^-$  and  $\mu^+\mu^-$  [77] provides a bound for a neutral resonance, which we identify here with the neutral state  $\rho^0$ . Figure 9 (left) shows the cross section prediction for  $\rho^0$

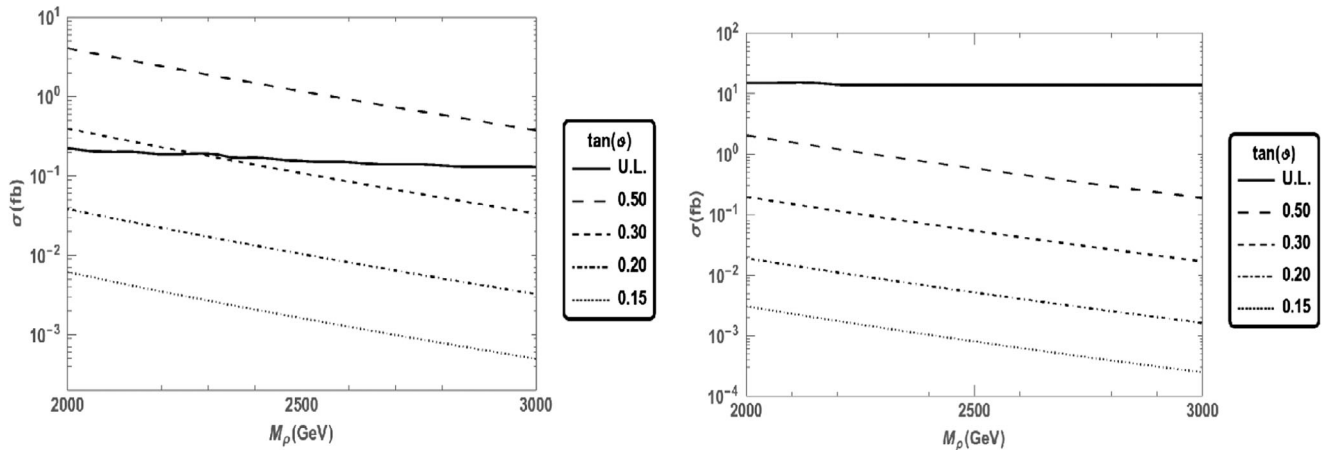


FIG. 9. Left: predicted  $pp \rightarrow \rho^0 \rightarrow l^+l^-$  resonant production at  $\sqrt{s} = 13$  TeV, for the combined channel  $ee$  and  $\mu\mu$ , as a function of  $M_\rho$ , for different values of  $\tan \vartheta$ ; the solid line is the 95% C.L. upper limit obtained by ATLAS [77]. Right: predicted  $pp \rightarrow \rho^0 \rightarrow \tau^+\tau^-$  resonant production at  $\sqrt{s} = 13$  TeV, for the combined channel  $ee$  and  $\mu\mu$ , as a function of  $M_\rho$ , for different values of  $\tan \vartheta$ ; the solid line is the 95% C.L. upper limit obtained by CMS [78].

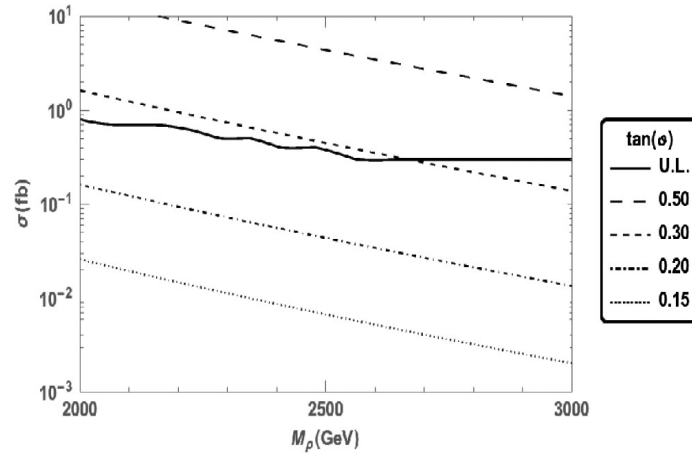


FIG. 10. Predicted  $pp \rightarrow \rho^\pm \rightarrow l\nu$  resonant production at  $\sqrt{s} = 13$  TeV, for  $l = e, \mu$ , as a function of  $M_\rho$ , for different values of  $\tan \vartheta$ ; the solid line is the 95% C.L. upper limit obtained by ATLAS [77].

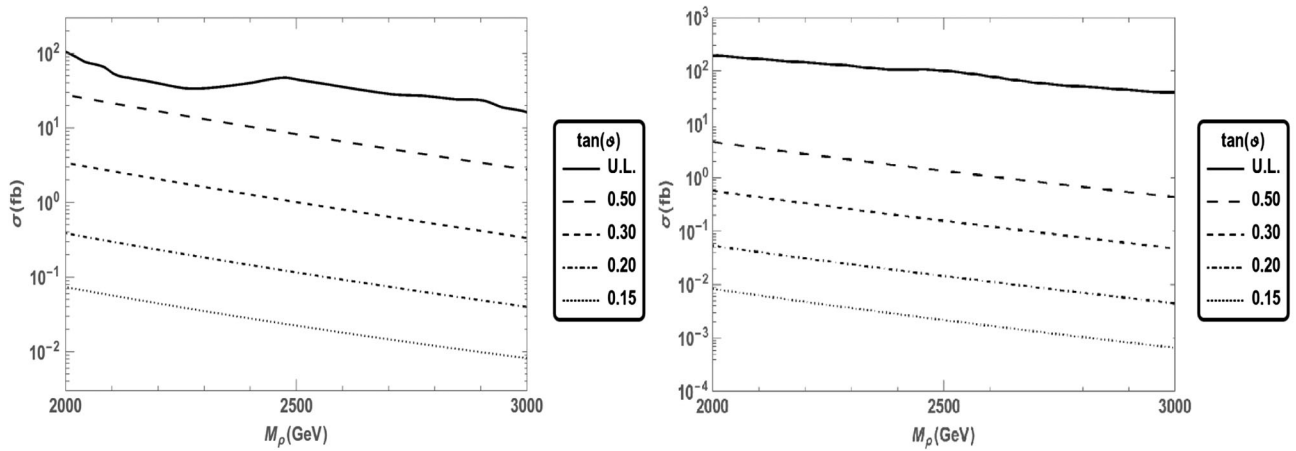


FIG. 11. Left: predicted  $pp \rightarrow \rho^{0,\pm} \rightarrow jj$  resonant production at  $\sqrt{s} = 13$  TeV as a function of  $M_\rho$ , for different values of  $\tan \vartheta$ ; the solid line is the 95% C.L. upper limit obtained by ATLAS [81]. Right: predicted  $pp \rightarrow \rho^0 \rightarrow t\bar{t}$  resonant production at  $\sqrt{s} = 13$  TeV, for the combined channel  $ee$  and  $\mu\mu$ , as a function of  $M_\rho$ , for different values of  $\tan \vartheta$ ; the solid line is the observed 95% C.L. upper limit obtained by ATLAS [80].

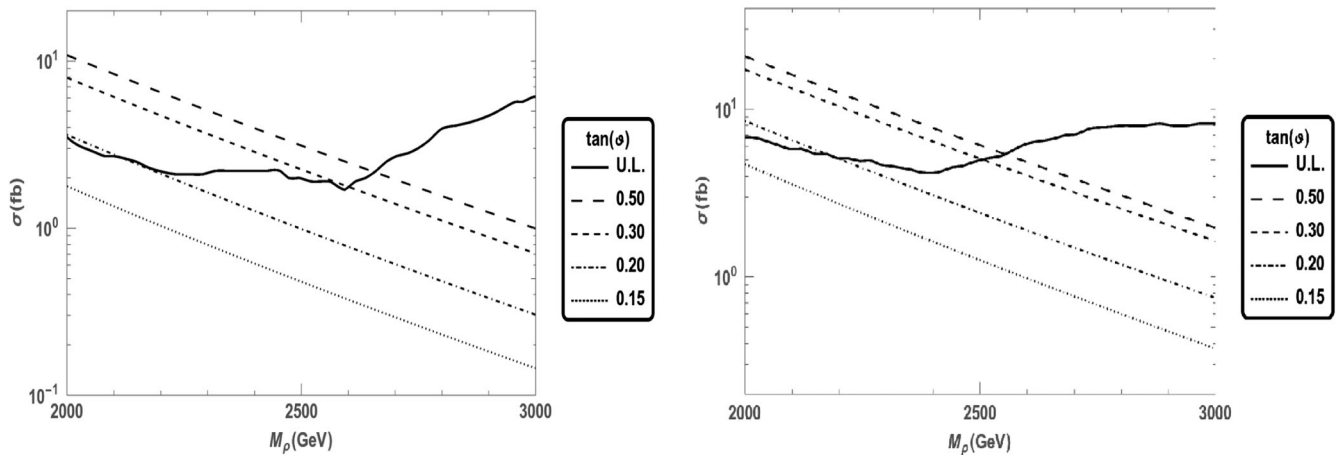


FIG. 12. Left: predicted  $pp \rightarrow \rho^0 \rightarrow ZH$  resonant production at  $\sqrt{s} = 13$  TeV as a function of  $M_\rho$ , for different values of  $\tan \vartheta$ . Right: predicted  $pp \rightarrow \rho^\pm \rightarrow W^\pm H$  resonant production at  $\sqrt{s} = 13$  TeV, for the combined channel  $ee$  and  $\mu\mu$ , as a function of  $M_\rho$ , for different values of  $\tan \vartheta$ . In both figures, the solid line is the observed 95% C.L. upper limit obtained by ATLAS [82].

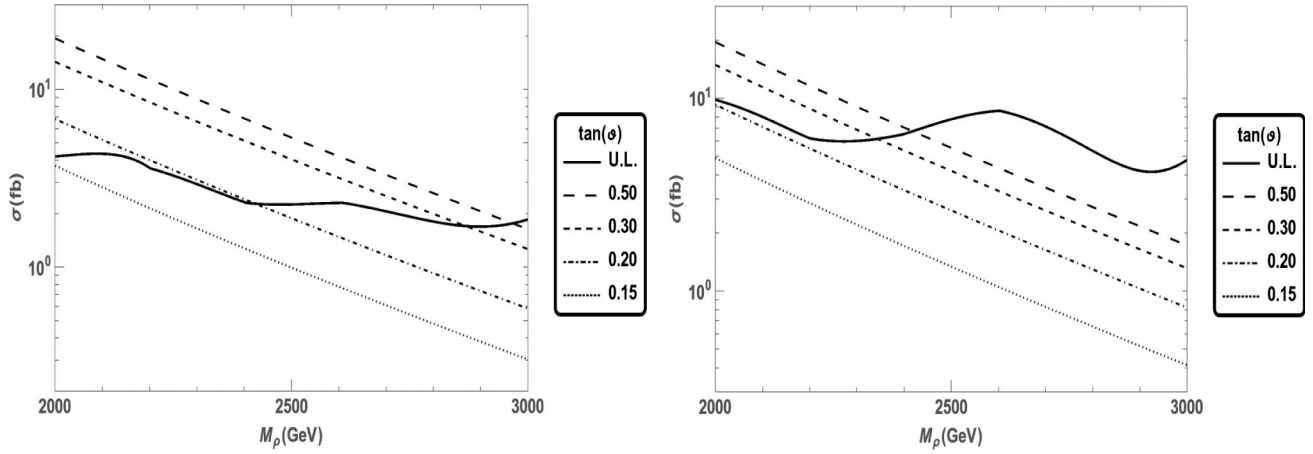


FIG. 13. Left: predicted  $pp \rightarrow \rho^0 \rightarrow W^+W^-$  resonant production at  $\sqrt{s} = 13$  TeV as a function of  $M_\rho$ , for different values of  $\tan \theta$ . Right: predicted  $pp \rightarrow \rho^\pm \rightarrow W^\pm Z$  resonant production at  $\sqrt{s} = 13$  TeV, for the combined channel  $ee$  and  $\mu\mu$ , as a function of  $M_\rho$ , for different values of  $\tan \theta$ . In both figures, the solid line is the 95% C.L. upper limit obtained by ATLAS [83].

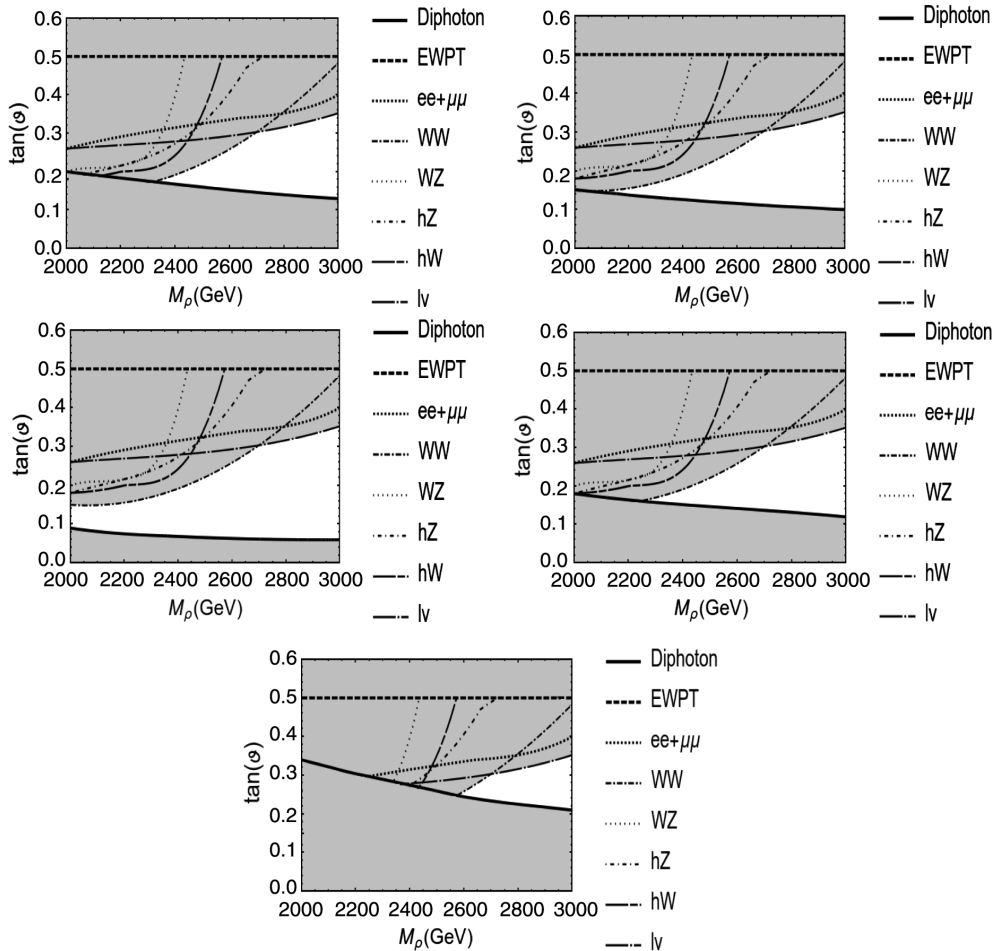


FIG. 14. Allowed and excluded regions in the model parameter space for different values of the  $\beta$  parameter after including all the constraints, i.e. the  $h \rightarrow \gamma\gamma$  (diphoton) constraint, the EWPT and the bounds from the LHC searches in the channels  $l^+l^-$ ,  $l\nu_l$  ( $l = e, \mu$ ),  $\tau^+\tau^-$ ,  $jj$ ,  $t\bar{t}$ ,  $ZH$ ,  $WH$ ,  $WW$  and  $WZ$ . The allowed region which is consistent with all the constraints is shown in white, while the grey regions are excluded. Here we have taken  $\beta = 4$  (upper left plot),  $\beta = 2$  (upper right plot),  $\beta = 0$  (middle left plot),  $\beta = -2$  (middle right plot),  $\beta = -4$  (lower plot).

decaying into dileptons ( $l = e, \mu$ ), together with the upper limit obtained by ATLAS, thus setting restrictions on the  $\tan \vartheta$  and  $M_\rho$  parameter space. The CMS upper bounds in the  $\tau^+\tau^-$  final state [78] are less restrictive than those of  $e^+e^-$  and  $\mu^+\mu^-$ , thus providing no further constraints as shown in Fig. 9 (right). The experimental bound in the  $l\nu$  final state, with  $l = e, \mu$ , is as stringent as in the  $l^+l^-$  channel (see Fig. 10). In contrast to dileptons, the  $t\bar{t}$  [80] and dijet [81] experimental upper bounds do not restrict our parameter space, as can be seen in Fig. 11.

Now, the associated  $hZ$  and  $hW^\pm$  production estimates and upper bounds [82] are shown in Fig. 12. Finally, the ATLAS constraints from  $ZW$  and  $W^+W^-$  production are shown in Fig. 13, in which again we contrast the experimental upper bound [83] with the resonant production of  $W^+W^-$  (left) and  $ZW$  (right).

Combining all these restrictions in the  $\tan \vartheta$ - $M_\rho$  plane, we arrive at Fig. 14, in which the allowed region of the parameter space is shown. Here, we include also the  $h \rightarrow \gamma\gamma$  (diphoton) constraint—which provides the lower bounds on  $\tan \vartheta$  and the upper bound from electroweak precision tests (EWPT)—which turns out to be less restrictive than the upper bounds from the dilepton and diboson channels, as shown in the figure.

## VII. CONCLUSIONS

We studied a framework of strongly interacting dynamics in which the Higgs (a scalar doublet) and also a heavy vector triplet appear as composite fields below a scale  $\Lambda \simeq 4\pi v \sim 3$  TeV. Without addressing details of the strong dynamics, we focus on the effective theory below the scale  $\Lambda$ , assumed to be the Standard Model, with its  $SU(2)_L \times U(1)_Y$  gauge group, with the addition of a  $SU(2)_L$  triplet of heavy vectors. The inclusion of the composite fields in the effective Lagrangian, i.e., the Higgs and the heavy vectors, is done by considering the vectors as gauge fields of a hidden local  $SU(2)_2$  symmetry and the Higgs as a doublet under this same symmetry. On the other hand, the SM gauge group at this stage is a  $SU(2)_1 \times U(1)$ . The SM fermions transform only under the latter group. By the mechanism of hidden local symmetry, the  $SU(2)_1 \times SU(2)_2$  breaks down to the diagonal  $SU(2)$  subgroup, which will be effectively the  $SU(2)_L$  of the SM.

This spontaneous breakdown is formulated in terms of a nonlinear sigma model, in which the “would-be Goldstone” bosons are absorbed into the massive vector triplets. In this process, the Higgs  $SU(2)_2$  doublet, which originally interacts with the composite vectors only, now acquires interactions with the SM fields. In this way, the composite Higgs maintains a rather strong interaction with the composite vector triplets and a weaker interaction with the SM fields.

We put to test the resulting spectrum and interactions, in view of the existing experimental data; we determined the constraints arising from the measured Higgs diphoton decay rate, electroweak precision tests, and the searches of heavy resonances at the LHC in the final states  $l^+l^-$  and  $l\nu_l$  ( $l = e, \mu$ ),  $\tau^+\tau^-$ ,  $jj$ ,  $t\bar{t}$ ,  $WZ$ ,  $WW$ ,  $WH$ , and  $ZH$ .

As a consequence of these constraints, we find that heavy vector masses in the range 2–3 TeV are consistent with the data, together with a mixing of the heavy vectors with the SM gauge bosons in the range  $\tan \vartheta \sim 0.1$ –0.3. These values are also consistent with the assumption that the Higgs couples weakly to the Standard sector and strongly to the heavy vector resonances.

We have found that the parameter of largest uncertainty is  $\beta$ , the bound of which cannot be isolated from current experimental results. Nevertheless, of the quantities we examined, only the Higgs diphoton decay rate at the LHC is sensitive to  $\beta$  to a significant level. Accordingly, we performed a scan of  $\beta$  in the range  $-4$  to  $4$ , finding that for all  $\beta$  values in that range there is always a region in the  $M_\rho - \tan \vartheta$  parameter space consistent with current experimental data.

Consequently, the current experimental data still allow for a Higgs boson that is strongly coupled to a composite sector, here assumed as triplet of vector resonances.

## ACKNOWLEDGMENTS

We would like to thank Felipe Rojas Abate, Martin Schmaltz, and J. Urbina for useful discussions. This work was supported in part by Conicyt (Chile) Grants Nos. ACT1406 and PIA/Basal FB0821 and by Fondecyt (Chile) Grants Nos. 1130617, 1170171, 1120346, 1160423, and 1170803. B. D. was partially supported by Conicyt Becas-Chile and PIIC/DGIP.

- 
- [1] G. Aad *et al.* (ATLAS Collaboration), *Phys. Lett. B* **716**, 1 (2012).  
 [2] S. Chatrchyan *et al.* (CMS Collaboration), *Phys. Lett. B* **716**, 30 (2012).  
 [3] K. A. Olive *et al.* (Particle Data Group), *Chin. Phys. C* **38**, 090001 (2014).

- [4] R. Contino, *Nuovo Cimento* **32**, 11 (2009).  
 [5] C. Grojean, *Proc. Sci.*, EPS-HEP2009, 008 (2009).  
 [6] R. Contino, arXiv:1005.4269.  
 [7] G. Panico and A. Wulzer, *Lect. Notes Phys.* **913**, 1 (2016).  
 [8] A. Arbey, G. Cacciapaglia, H. Cai, A. Deandrea, S. Le Corre, and F. Sannino, *Phys. Rev. D* **95**, 015028 (2017).

- [9] K. Agashe, R. Contino, and A. Pomarol, *Nucl. Phys.* **B719**, 165 (2005).
- [10] B. Gripaios, A. Pomarol, F. Riva, and J. Serra, *J. High Energy Phys.* **04** (2009) 070.
- [11] R. Barbieri, B. Bellazzini, V. S. Rychkov, and A. Varagnolo, *Phys. Rev. D* **76**, 115008 (2007).
- [12] C. Csaki, A. Falkowski, and A. Weiler, *J. High Energy Phys.* **09** (2008) 008.
- [13] R. Contino, D. Marzocca, D. Pappadopulo, and R. Rattazzi, *J. High Energy Phys.* **10** (2011) 081.
- [14] J. Mrazek, A. Pomarol, R. Rattazzi, M. Redi, J. Serra, and A. Wulzer, *Nucl. Phys.* **B853**, 1 (2011).
- [15] A. Pomarol and F. Riva, *J. High Energy Phys.* **08** (2012) 135.
- [16] R. Contino, M. Ghezzi, C. Grojean, M. Muhlleitner, and M. Spira, *J. High Energy Phys.* **07** (2013) 035.
- [17] D. Pappadopulo, A. Thamm, and R. Torre, *J. High Energy Phys.* **07** (2013) 058.
- [18] M. Montull, F. Riva, E. Salvioni, and R. Torre, *Phys. Rev. D* **88**, 095006 (2013).
- [19] G. Cacciapaglia and F. Sannino, *J. High Energy Phys.* **04** (2014) 111.
- [20] M. Carena, L. Da Rold, and E. Pontón, *J. High Energy Phys.* **06** (2014) 159.
- [21] G. von Gersdorff, E. Pontón, and R. Rosenfeld, *J. High Energy Phys.* **06** (2015) 119.
- [22] A. Belyaev, G. Cacciapaglia, H. Cai, T. Flacke, A. Parolini, and H. Serôdio, *Phys. Rev. D* **94**, 015004 (2016).
- [23] G. Cacciapaglia, H. Cai, A. Deandrea, T. Flacke, S. J. Lee, and A. Parolini, *J. High Energy Phys.* **11** (2015) 201.
- [24] S. Fichtel, G. von Gersdorff, E. Pontón, and R. Rosenfeld, *J. High Energy Phys.* **09** (2016) 158.
- [25] S. Fichtel, G. von Gersdorff, E. Pontón, and R. Rosenfeld, *J. High Energy Phys.* **01** (2017) 012.
- [26] Y. Wu, B. Zhang, T. Ma, and G. Cacciapaglia, *J. High Energy Phys.* **11** (2017) 058.
- [27] W. A. Bardeen, C. T. Hill, and M. Lindner, *Phys. Rev. D* **41**, 1647 (1990).
- [28] K. Lane and A. Martin, *Phys. Lett. B* **635**, 118 (2006).
- [29] G. F. Giudice, C. Grojean, A. Pomarol, and R. Rattazzi, *J. High Energy Phys.* **06** (2007) 045.
- [30] A. R. Zerwekh, *Eur. Phys. J. C* **46**, 791 (2006).
- [31] Y. Bai, M. Carena, and E. Pontón, *Phys. Rev. D* **81**, 065004 (2010).
- [32] K. Lane and A. Martin, *Phys. Rev. D* **80**, 115001 (2009).
- [33] A. R. Zerwekh, *Eur. Phys. J. C* **70**, 917 (2010).
- [34] A. E. Carcamo Hernandez and R. Torre, *Nucl. Phys.* **B841**, 188 (2010).
- [35] A. E. Carcamo Hernandez, *Eur. Phys. J. C* **72**, 2154 (2012).
- [36] A. E. Carcamo Hernandez, [arXiv:1108.0115](https://arxiv.org/abs/1108.0115).
- [37] G. Burdman and C. E. F. Haluch, *J. High Energy Phys.* **12** (2011) 038.
- [38] E. Eichten, K. Lane, and A. Martin, [arXiv:1210.5462](https://arxiv.org/abs/1210.5462).
- [39] A. E. Carcamo Hernandez, C. O. Dib, N. A. Neill, and A. R. Zerwekh, *J. High Energy Phys.* **02** (2012) 132.
- [40] B. Bellazzini, C. Csaki, J. Hubisz, J. Serra, and J. Terning, *J. High Energy Phys.* **11** (2012) 003.
- [41] B. Díaz and A. R. Zerwekh, *Int. J. Mod. Phys. A* **28**, 1350133 (2013).
- [42] O. Castillo-Felisola, C. Corral, M. González, G. Moreno, N. A. Neill, F. Rojas, J. Zamora, and A. R. Zerwekh, *Eur. Phys. J. C* **73**, 2669 (2013).
- [43] A. E. Cárcamo Hernández, C. O. Dib, and A. R. Zerwekh, *Nuovo Cimento C* **036**, 177 (2013).
- [44] A. E. Carcamo Hernandez, C. O. Dib, and A. R. Zerwekh, *Eur. Phys. J. C* **74**, 2822 (2014).
- [45] A. E. Carcamo Hernandez, C. O. Dib, and A. R. Zerwekh, *Nucl. Part. Phys. Proc.* **267–269**, 35 (2015).
- [46] D. Pappadopulo, A. Thamm, R. Torre, and A. Wulzer, *J. High Energy Phys.* **09** (2014) 060.
- [47] K. Lane, *Phys. Rev. D* **90**, 095025 (2014).
- [48] K. Lane and L. Pritchett, *Phys. Lett. B* **753**, 211 (2016).
- [49] K. Lane and L. Pritchett, *J. High Energy Phys.* **06** (2017) 140.
- [50] M. Gintner and J. Juráň, *Eur. Phys. J. C* **76**, 651 (2016); **77**, 6(E) (2017).
- [51] S. Di Chiara, M. Heikinheimo, and K. Tuominen, *J. High Energy Phys.* **03** (2017) 009.
- [52] R. Foadi, M. T. Frandsen, T. A. Rytto, and F. Sannino, *Phys. Rev. D* **76**, 055005 (2007).
- [53] T. A. Rytto and F. Sannino, *Phys. Rev. D* **78**, 115010 (2008).
- [54] F. Sannino, *Acta Phys. Pol. B* **40**, 3533 (2009).
- [55] A. Belyaev, M. S. Brown, R. Foadi, and M. T. Frandsen, *Phys. Rev. D* **90**, 035012 (2014).
- [56] T. Hapola and F. Sannino, *Mod. Phys. Lett. A* **26**, 2313 (2011).
- [57] R. Foadi, M. T. Frandsen, and F. Sannino, *Phys. Rev. D* **87**, 095001 (2013).
- [58] M. Chala, G. Durieux, C. Grojean, L. de Lima, and O. Matsedonskyi, *J. High Energy Phys.* **06** (2017) 088.
- [59] D. D. Dietrich, F. Sannino, and K. Tuominen, *Phys. Rev. D* **72**, 055001 (2005).
- [60] M. A. Shifman, A. I. Vainshtein, M. B. Voloshin, and V. I. Zakharov, *Yad. Fiz.* **30**, 1368 (1979) [*Sov. J. Nucl. Phys.* **30**, 711 (1979)].
- [61] M. B. Gavela, G. Girardi, C. Malleville, and P. Sorba, *Nucl. Phys.* **B193**, 257 (1981).
- [62] P. Kalyniak, R. Bates, and J. N. Ng, *Phys. Rev. D* **33**, 755 (1986).
- [63] J. F. Gunion, H. E. Haber, G. L. Kane, and S. Dawson, *The Higgs Hunter's Guide*, Frontiers in Physics (Westview Press, Boulder, 2000).
- [64] M. Spira, *Fortschr. Phys.* **46**, 203 (1998).
- [65] A. Djouadi, *Phys. Rep.* **459**, 1 (2008).
- [66] W. J. Marciano, C. Zhang, and S. Willenbrock, *Phys. Rev. D* **85**, 013002 (2012).
- [67] L. Wang and X. F. Han, *Phys. Rev. D* **86**, 095007 (2012).
- [68] M. D. Campos, A. E. Cárcamo Hernández, H. Päs, and E. Schumacher, *Phys. Rev. D* **91**, 116011 (2015).
- [69] A. E. Cárcamo Hernández, I. de Medeiros Varzielas, and E. Schumacher, *Phys. Rev. D* **93**, 016003 (2016).
- [70] V. Khachatryan *et al.* (CMS Collaboration), *Eur. Phys. J. C* **74**, 3076 (2014).
- [71] G. Aad *et al.* (ATLAS Collaboration), *Phys. Rev. D* **90**, 112015 (2014).
- [72] M. E. Peskin and T. Takeuchi, *Phys. Rev. D* **46**, 381 (1992).
- [73] G. Altarelli and R. Barbieri, *Phys. Lett. B* **253**, 161 (1991).
- [74] R. Barbieri, A. Pomarol, R. Rattazzi, and A. Strumia, *Nucl. Phys.* **B703**, 127 (2004).

- [75] M. Baak, M. Goebel, J. Haller, A. Hoecker, D. Ludwig, K. Moenig, M. Schott, and J. Stelzer, *Eur. Phys. J. C* **72**, 2003 (2012).
- [76] A. Belyaev, N.D. Christensen, and A. Pukhov, *Comput. Phys. Commun.* **184**, 1729 (2013).
- [77] ATLAS Collaboration, Report No. ATLAS-CONF-2017-027.
- [78] V. Khachatryan *et al.* (CMS Collaboration), *J. High Energy Phys.* **02** (2017) 048.
- [79] M. Aaboud *et al.* (ATLAS Collaboration), [arXiv:1706.04786](https://arxiv.org/abs/1706.04786).
- [80] ATLAS Collaboration, Report No. ATLAS-CONF-2016-014.
- [81] ATLAS Collaboration, Report No. ATLAS-CONF-2016-069.
- [82] ATLAS Collaboration, Report No. ATLAS-CONF-2017-018.
- [83] ATLAS Collaboration, Report No. ATLAS-CONF-2016-062.